Radiation processes of impurities and hydrogen in detached divertor plasmas of JT-60U

T. Nakano, H. Kubo, N. Asakura, K. Shimizu, S. Konoshima, K. Fujimoto, H. Kawashima and S. Higashijima

Japan Atomic Energy Agency, Naka, Ibaraki-ken, 311-0193 Japan

e-mail contact of main author: nakano.tomohide@jaea.go.jp

Abstract. Volume recombination of C^{4+} and e^- into C^{3+} is observed for the first time in detached plasmas with MARFE. It is found that the recombination flux of C^{4+} to C^{3+} is comparable to the ionization flux of C^{3+} to C^{4+}, and that the recombination zone is above an X point and beneath the ionization zone. This result suggests that this volume recombination predominantly produces C^{3+} ions, which contribute 60-80 % to the total radiation power in the divertor plasma.

1 Introduction

In high-density divertor plasmas, an X-point MARFE is often formed, which is characterized by an appearance of the toroidally-symmetric, intense-radiation band around a magnetic null point (an X-point). It has been found that the electron temperature and density are, respectively, lower than 1 eV and higher than $1 \times 10^{20}\mathrm{m}^{-3}$, and that the volume recombination flux of hydrogen ion is comparable to the ionization flux of neutral hydrogen. The radiation power of hydrogen contributes 20-40 % at most to the total radiation power from the divertor plasma. The rest of the radiation power (more than 80-60 %) is ascribed to impurities, in particular, C^{3+} in carbon based devices [1, 2]. It has been considered that the source of C^{3+} is ionization of C^{2+} because the recombination of impurities has NOT been observed. This paper points out that the predominant source of C^{3+} is volume recombination of C^{4+} and e^- for the first time.

2 Experimental

The discharge conditions for the present spectroscopic measurement were as follows: a plasma current of 1.5 MA, a toroidal magnetic field of 3.5 T, a neutral beam heating power of 4.3 MW, and a line-averaged electron density of the core plasma of 3.5×10^{19} m^{-3}, which was kept constant by a feedback control system of a gas-puffing rate.

The spectroscopic system consists of an object optics, two parallel arrays of sixty optical fibers (vertical), one array of thirty two opticla fibers (horizontal) and three visible spectrometers.

The object optics covers the divertor region with a spatial resolution of $\sim$ 1 cm vertically and

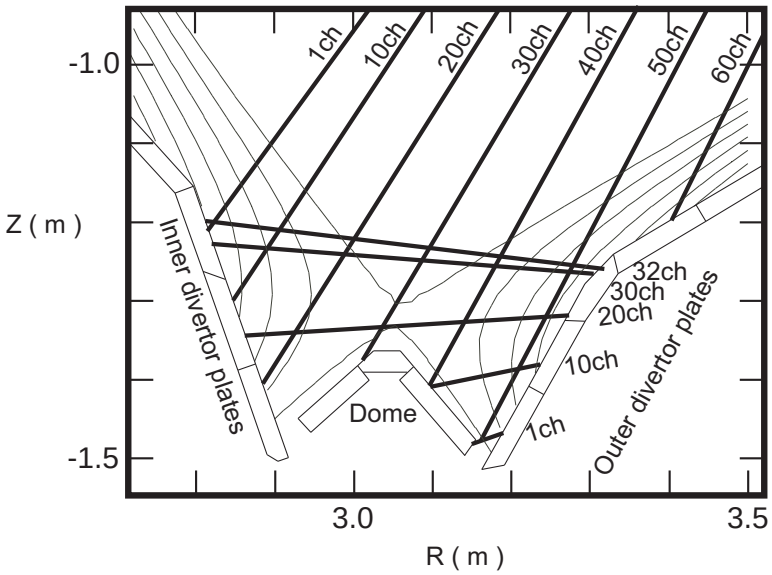

FIG. 1: Viewing chords (vertical 60 ch, and horizontal 32 ch) for the spectroscopic measurement, the magnetic configuration and the divertor structures.

horizontally as shown in Fig.1. Emission from the divertor plasma is collimated with two lenses onto the optical fibers. Then the light is transmitted to a diagnostic room through the optical fibers. In the diagnostic room, ten optical fibers of the vertical array,and sixty and thirty two optical fibers of the viertical and the horizontal array are guided to a high wavelength resolution spectrometer and a low wavelength resolution spectrometer, respectively.
The high wavelength resolution spectrometer observed ten spectra of C IV ($n = 6 - 7$) around 772.6 nm, simultaneously, where n denotes a principal quantum number. This spectrometer is built in the Littrow mounting with an echelle grating. The Littrow lens (focal length 1.2 m and diameter 100 mm) is used for suppression of the astigmatic images of the optical fibers. The echelle grating (79 grooves/mm, height 102 mm and width 254 mm, and blazing angle 74°) is used for high wavelength resolution, which is obtained in high spectral order. The spectral line of C IV ($n = 6 - 7$) is observed in the 32nd spectral order in the case that the angle of the echelle grating is set so as to obtain the highest diffraction efficiency. A charge coupled device (CCD) camera with an image-intensifier is used as a detector. The CCD camera has 512×512 pixels with an effective size of 24×24 μm, and the quantum efficiency of the image-intensifier is $\sim 40\%$ around 772.6 nm.
A low resolution spectromter observed 92 spectra of C IV ($3s^2S - 3p^2P$) and C IV (n=6-7) along the viewing chord shown in Fig 1, simultaneously. Two camera lenses are built in to suppress astigmatic images of the optical fiber, and a grating with 150 grooves /mm is used. A back-illuminated CCD camera having 1340×1300 pixels with a size of $20 \times 20\mu$m is used as a detector, and the quantum efficiency is $\sim 80\%$ around 772.6 nm.

3 Results

3.1 Stark Broadening of C IV (n=6-7)

While the MARFE was maintained, a spectral profile of C IV (n = 6 - 7), shown in Fig. 2, was taken along the viewing chord of 31 ch, which penetrated the vicinity of the magnetic null point (the X-point), as shown in Fig. 1. After the MARFE occurrence, the spectral profile of C IV (n = 6 - 7) from the MARFE region became broader, in particular, around the tails of the spectrum compared with those from the other region and those from the X-point before the MARFE occurrence. The spectral profile was reproduced by a Voigt function, which is convolution of a Gaussian and a Lorentzian function. On the assumption that the broadenings fitted by a Gaussian and a Lorentzian function were ascribed to the Doppler and the Stark effect, respectively, the cor-

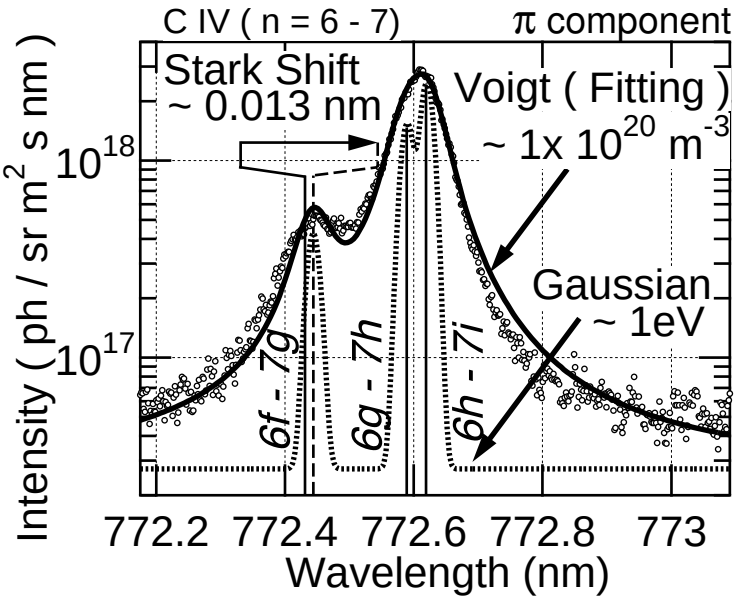

FIG. 2: Spectral profile of C IV (n = 6 - 7) from the MARFE region. The spectrum is composed of three transitions, $6f-7g$, $6g-7h$ and $6h-7i$, whose wavelength and relative gA value are indicated by, respectively, the location and the length of the vertical lines. The result of regression analysis with a Voigt function is shown by a solid curve, and its Gaussian component by a dotted curve.

responding ion temperature and electron density were ~ 1 eV and $\sim 1 \times 10^{20}$ m^{-3}, respectively. Given that the electron density is 1×10^{20} m^{-3}, the Holtzmark formula yields an electric field of 0.8 kV/cm. In this electric field, $C^{3+}(n = 7)$ is perturbed with energy of ~ 0.2 cm^{-1}. Because this perturbation energy is comparable to the energy difference, for example, between $7h$ and $7i$, the Stark effect can affects these energy levels. This was confirmed for the Stark shift of C IV ($6f$ - $7g$). The calculated Stark shift ($\sim$ 0.01 nm) was in good agreement with the measured (0.013 ± 0.003 nm) as shown in Fig. 2 by the dashed vertical line.

3.2 Volume recombination of C^{4+} and e^-

From the intensities of C IV ($3s^2S - 3p^2P$) and C IV (n=6-7), the line-integral population densities of the upper levels, $C^{3+}(3p^2P_{3/2})$ and $C^{3+}(n$=7) were estimated. As shown in Fig. 3 (a), these three population densities had maxima around a viewing chord 29 ch, which viewed the vicinity of the X-point, and decreased away from the X-point to the strike points. In particular, the population densities of $C^{3+}(n = 7)$ and $C^{3+}(n = 6)$ decreased significantly. Figure 3 (b) shows the population ratio of $C^{3+}(n = 7)$ to $C^{3+}(3p^2P_{3/2})$. This population ratio had a peak of 0.1 - 0.01 around the X-point, and decreased to 0.01 - 0.001 away from the X-point. The population ratio of $C^{3+}(n = 7)$ to $C^{3+}(3p^2P_{3/2})$ was investigated to determine which process populated $C^{3+}(n = 7)$ predominantly, excitation from the ground state of C^{3+} or recombination of C^{4+} and electron. The measured population ratio was compared with the population ratio calculated by a collisional-radiative model [3] shown in Fig. 4. At an electron density of 1×10^{20} m^{-3} and an electron temperature of 1 eV, which are obtained from the regression analysis of C IV (n = 6 - 7) shown in Fig. 2, the measured population ratio (0.01 - 0.1

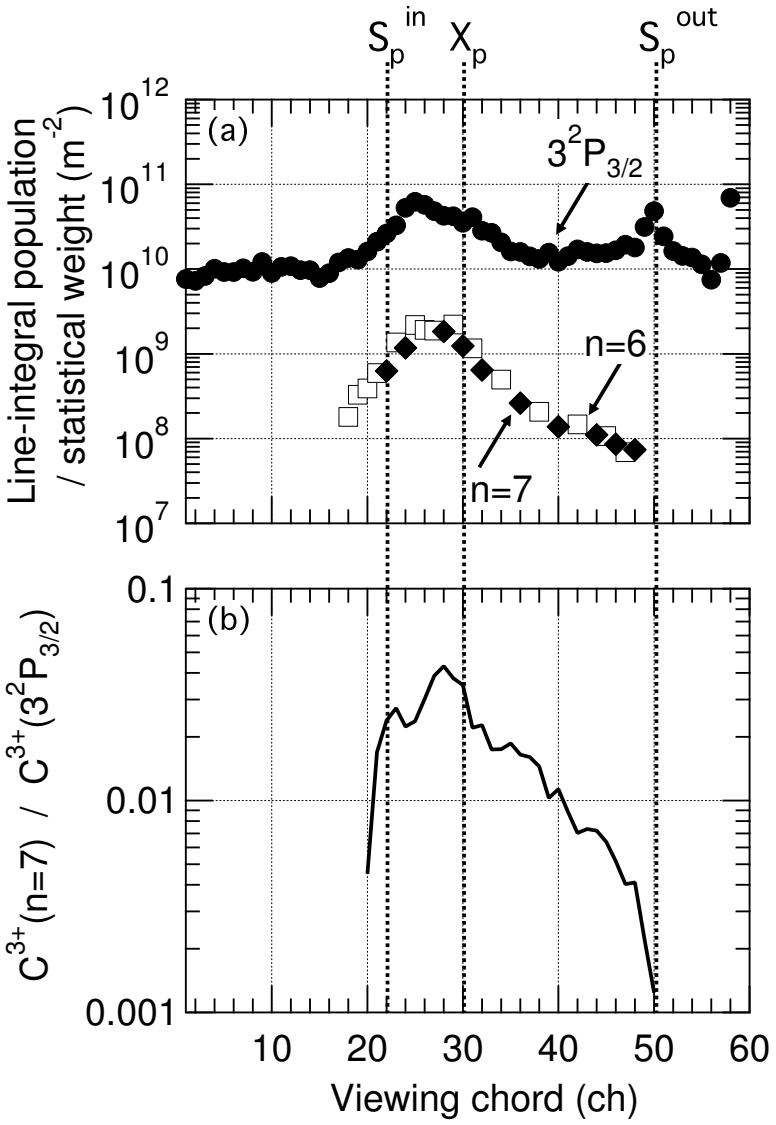

FIG. 3: (a) Line-integral population densities of $C^{3+}(n = 7)$, $C^{3+}(n = 6)$ and $C^{3+}(3p^2P_{3/2})$ and (b) population ratio of $C^{3+}(n = 7)$ to $C^{3+}(3p^2P_{3/2})$ as a function of the viewing chord number. The X-point, the inner and the outer strike point are indicated by X_p, S_p^{in} and S_p^{out}, respectively.

) around the X-point was not explained by only the ionizing-population component. Hence, the measured population ratio around the X-point was considered to indicate the recombination of C^{4+} with electron. But the measured population ratio was smaller by about one order than the calculated population ratio of the recombining component. This discrepancy between the measurement and the calculation might be interpreted as follows : in the region except for the X-point, $C^{3+}(3p^2P_{3/2})$ was dominated by the ionizing component as shown in Fig. 4, and the ionizing component of $C^{3+}(3p^2P_{3/2})$ was also considered to exist around the X-point. Because the viewing chord passed the plasma with the ionizing component, the measured population density of $C^{3+}(3p^2P_{3/2})$ was considered to include the ionizing component, resulting in smaller population ratio than predicted by the calculation. From the above discussion, it is concluded that the recombination of C^{4+} with electron was identified around the X-point.

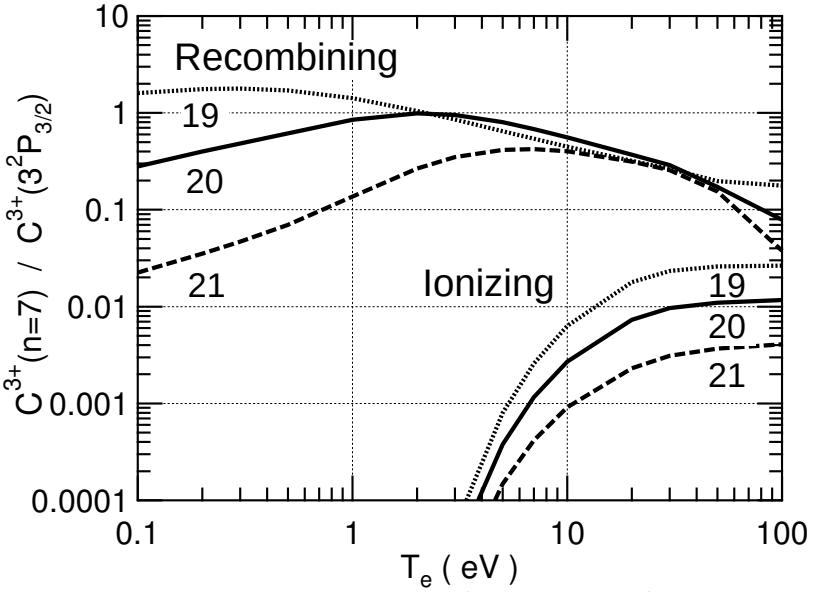

FIG. 4: Calculated population ratio of $C^{3+}(n = 7)$ to $C^{3+}(3p^2P_{3/2})$ as a function of electron temperature. The recombining and the ionizing component are shown separately. Numbers beside the curves indicate the power of ten of the electron density. The hatched region indicates the population ratio measured around the X-point, and the shaded region the population ratio in the other region.

3.3 2 dimensinal structure of the volume recombination

The recombination flux of C^{4+} and e^- is evaluated from the intensity of C IV (n = 6 7), multiplied by 20, calculated by the collisional-radiative model [3] at electron temperature and density of 1 eV and $1 \times 10^{20}\mathrm{m}^{-3}$, respectively. Figure 5 shows a 2 dimensional structure of the recombination flux, reconstructed by a computer tomography technique. The recombination flux is localized above the X-point. The line integral recombination flux is $\sim 2\times10^{20}\mathrm{m}^{-2}\mathrm{s}^{-1}$ along the viewing chord passing through the peak of the recombination zone. A similar analysis for C IV ($3s^2S - 3p^2P$) indicates that the ionization zone of C^{3+} is positioned over the recombination zone of C^{4+}, and that the ionization flux is comparable with the recombination flux. Because predominant emission of C IV ($3s^2S - 3p^2P$) is not observed below the X-point, the C^{3+} ions produced through the recombination of C^{4+} and e^- is considered to be transported upward, resulting in C IV ($3s^2S - 3p^2P$) emission at relatively high temperature region (20 eV).

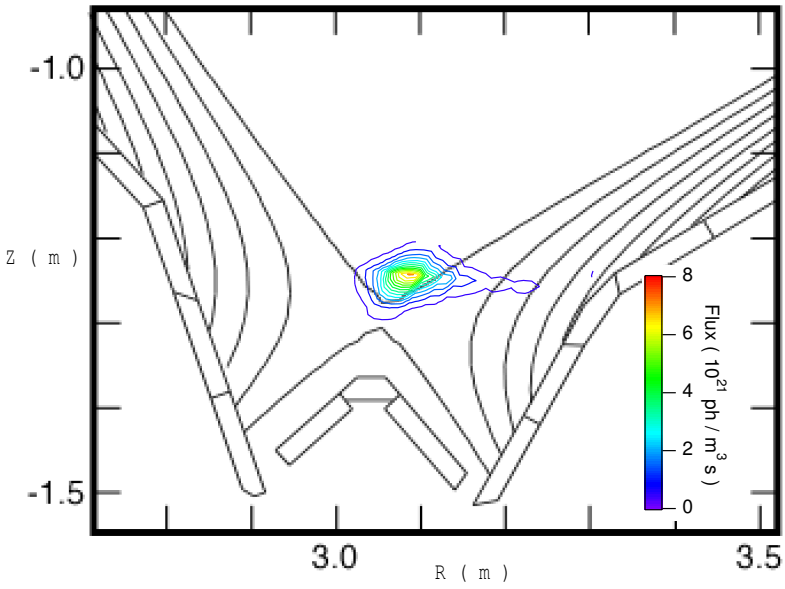

FIG. 5: Recombination flux of C^{4+} to C^{3+}, reconstructed by a computer tomography technique from C IV (n = 6-7) line measured with 92 viewing chords, shown in Fig. 1.

3.4 Radiation power with the volume recombination process

The radiation power rate coefficient for the recombination component, $L^{recomb}_{C^{3+}}$, calculated by the collisional-radiative model [3] at an electron temperature and density of 1 eV and $1 \times 10^{20}\mathrm{m}^{-3}$ is $9.1\times10^{-33}(\mathrm{Wm}^3)$. Because $C^{3+}(n = 7)$ is dominated by the recombination, $n_{C^{3+}(n=7)} = R_0 n_e n C^{4+}$, where R_0 is $2.7 \times 10^{-27}(\mathrm{m}^3)$. And the line-integral population density, $nC^{3+}(n = 7)l$, is measured as $1.8\times10^{9}(\mathrm{m}^{-2})$. From these values, the radiation power from the recombination component, $P^{recomb}_{C^{3+}}$ is calculated as fol-

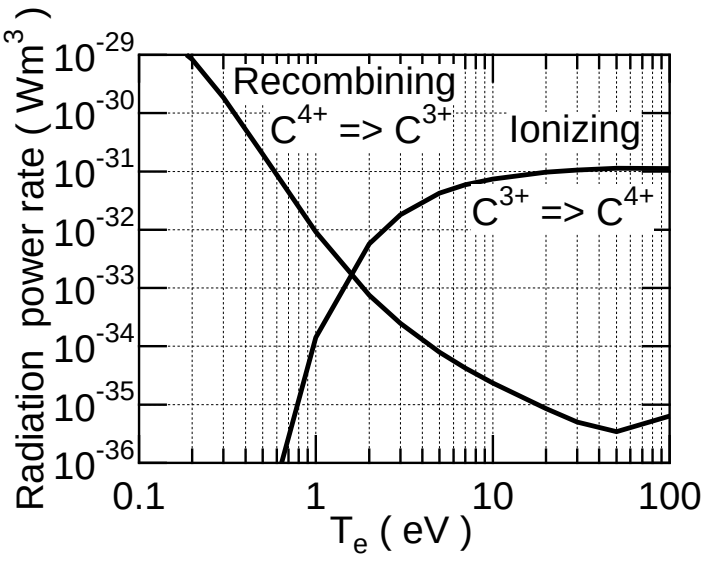

FIG. 6: Radiation power rate coefficient of the ionizing and the recombining component as a function of electron temperature at an electron density of 1×10^{20} m^{-3}.

lows:

$$\begin{aligned} P_{recomb}^{C^{3+}} &= L_{recomb}^{C^{3+}} \cdot n_e \cdot n_{C^{4+}} \cdot L \\ &= L_{recomb}^{C^{3+}} \cdot n_{C^{3+}(n=7)} \cdot L/R_0 \\ &= 9.1 \times 10^{-32}\ (\mathrm{Wm^3}) \cdot 1.2 \times 10^{9}\ (\mathrm{m^{-2}})/2.7 \times 10^{-27}\ (\mathrm{m^3}) \\ &= 6.0(kW/m^2) \end{aligned}$$

This radiation power is less than 1 % of the total radiation power, measured by a bolometer (1.1 MW/m^2). From a similar analysis for $C^{3+}(3p^2P)$, the radiation power from the ionization component is evaluated to be 0.70 (MW/m^2) on the assumption that the electron temperature is 20 eV. From the above discussion, although the radiation power with the recombination process is low, the C^{3+} ions, produced by the recombination, contribute 64 % of the total radiation.

4 Summary

When a MARFE was formed around the X-point, the spectral profile of C IV (n=6-7) taken along the viewing chord for the X-point became broader due to the Stark effect compared to those along other viewing chord and those before the MARFE occurrence. From regression analysis of the spectral profile, temperature and density were estimated to be 1 eV and 1×10^{20} m^{-3}, respectively. From comparison of the measured and the calculated population ratio of C^{3+}(n=7) to $C^{3+}(3p^2P_{3/2})$, it is concluded that volumetric recombination of C^{4+} with electron was identified at the vicinity of the X-point. Although the line-integral radiation power due to the volume recombination is only 1 % of the total radiation power along the same viewing chord, the recombination produces the C^{3+} ions, which contribute 64 % of the total radiation. The above result suggests that the recombination process contributed to cooling of the divertor plasma.

Reference

[1] H. Kubo, T. Sugie *et al*., Plasma Phys. Control. Fusion, **37** (1995) 1133.

[2] M. E. Fenstermacher, S. L. Allen *et al*., Phys. Plasmas, **4** (1997) 1761.

[3] T. Nakano, H. Kubo *et al*., J. Plasma and Fusion Res., **80** (2004) 500.